Mars orbital synthetic aperture radar: Obtaining geologic information from radar polarimetry

Bruce A. Campbell and Ted A. Maxwell

Center for Earth and Planetary Studies, Smithsonian Institution, Washington, D. C., USA

Anthony Freeman

Jet Propulsion Laboratory, Pasadena, California, USA

[1]   Radar penetration of mantling layers, and scattering from buried objects or interfaces, is a topic of current interest in both terrestrial and planetary remote sensing. We examine the behavior of surface and subsurface scattering interfaces and the types of information that may be obtained from observations in different polarizations and wavelengths. These results are applied to the design of a future Mars orbital synthetic aperture radar (SAR), for which we draw the following conclusions. (1) Mapping of buried geologic features is best accomplished using VV polarization, at an optimal wavelength determined by the competing effects of antenna gain, attenuation in the dust, and the reduction in effective surface roughness with wavelength. P band frequencies ($\sim$1 GHz or less) offer the best opportunity for detection of moderately rough, buried features. (2) The relative roles of surface and subsurface scattering may be determined using measurements in HH and VV polarization, with a channel gain calibration better than 0.5 dB. (3) The thickness of a mantling layer (or ice mass) cannot be directly inferred from multiwavelength observations. Layer thickness may be inferred from the interferometric correlation of backscatter measurements collected on suitably spaced orbital passes, though the required phase measurement accuracy is challenging. While additional information may be gained by collecting scattering data in more polarizations or wavelengths, we suggest that the primary science goals of a Mars-orbiting radar could be accomplished by a single-wavelength system capable of collecting VV and HH polarizations with the calibration and orbit control needed to permit interferometric analysis.   INDEX TERMS: 5464 Planetology: Solid Surface Planets: Remote sensing; 5470 Planetology: Solid Surface Planets: Surface materials and properties; 5494 Planetology: Solid Surface Planets: Instruments and techniques; KEYWORDS: Mars, radar

1. Introduction

[2] Radar remote sensing provides complementary information to visible and infrared observations of planetary surfaces. In some cases, such as for Venus or Titan, synthetic aperture radar (SAR) may be the only method of obtaining high-resolution maps of cloud-covered terrain. Typically, such applications utilize radar signals with wavelengths on the order of 1–10 cm, and the backscattered return is modulated largely by surface roughness. For Mars, imaging radar operating at longer wavelengths (tens of centimeters) can penetrate the surficial dust mantle to reveal buried fluvial, volcanic, or ice-related features. A Mars orbital radar-mapping mission is within the scope of the current NASA Scout Program [Campbell et al., 2001, 2004].

[3] Much of the existing work on radar penetration and subsurface scattering in terrestrial settings relates to ice sheets and arid desert regions, since only in very "dry" targets will a radar signal penetrate to significant depths [e.g., Schaber et al., 1986, 1997; Farr et al., 1986; Haldemann and Muhleman, 1999; Williams and Greeley, 2001; Paillou et al., 2003]. Earth-based radar studies of volume scattering include analyses of lunar mare basalt composition and buried rough ejecta, subsurface returns from beneath fine-grained mantling deposits on Venus, ice caps on Mars, the icy shells of the Galilean satellites, and identification of ice in polar craters on Mercury [e.g., Schaber et al., 1975; Thompson et al., 1979; Carter et al., 2004; Muhleman et al., 1991; Ostro et al., 1992; Harmon et al., 1994]. While these studies provide a strong rationale for the science value of a Mars orbital radar mapper, there is a need to evaluate the technical approach to such observations. For example, Earth-observing radar systems, such as the NASA/JPL AIRSAR

or the Shuttle Imaging Radar C (SIR-C), collect the full scattering matrix (HH, VV, HV, and VH polarization amplitudes and phases) for each resolution cell at any given wavelength. Such systems permit maximum flexibility in analyzing the scattering properties of a target but entail data volumes that may be impractical for regional or global mapping of planetary surfaces. It is therefore important to consider the combinations of radar wavelength and polarization that are most useful in characterizing subsurface geologic features.

[4] Radar scattering from even a "simple" surface, described by a sharp dielectric discontinuity, a nonscattering subsurface medium, and a statistical distribution of surface heights or slopes (roughness), can pose significant challenges for theoretical modeling. In general, analytical solutions exist only for slightly rough surfaces (the "small-perturbation" regime) and for gentle undulations on scales many times that of the illuminating wavelength (the "Kirchhoff" regime) [e.g., *Ulaby et al.*, 1982]. The radar-scattering behavior of mantled surfaces is even more complicated, since we must also consider the transmission, attenuation, and subsurface scattering of incident energy. Remote sensing thus poses a highly underdetermined problem, encompassing a broad spectrum of possible surface and subsurface physical properties. Fortunately, there are reasonable assumptions, based on empirical analysis, that limit these degrees of freedom and permit useful information to be extracted from multipolarization measurements. In particular, we exploit the ratios between echoes in various polarization states.

[5] The purpose of this paper is to develop a relatively simplistic, but plausible, physical representation of mantled geologic surfaces and examine the associated range of radar polarization behaviors as a function of incidence angle and wavelength. We use the results to define "baseline" capabilities for a Mars orbital radar system. In sections 2 and 3 we introduce our nomenclature for surface and subsurface properties and discuss the degrees of freedom in multipolarization radar data. Section 4 reviews polarization behavior in radar scattering from rough surfaces, and section 5 follows a parallel analysis for subsurface scattering. Section 6 considers the attenuation and polarization effects of a mantling layer on backscattered radar signals. Section 7 shows how these models may be used to constrain the design of a Mars orbital radar system.

2. Constitutive and Roughness Properties

[6] Our idealized model for the near-surface environment of Mars is described by the following characteristics (Figure 1): (1) a homogeneous, fine-grained mantling layer of thickness h, with real dielectric constant ε_s', imaginary dielectric constant ε_s'', loss tangent $\tan\delta_s = \varepsilon_s''/\varepsilon_s'$, and an upper interface of some roughness and (2) a rough basal scattering surface and/or suspended population of buried objects, with real dielectric constant ε_b'. In the most general sense, the subsurface may be characterized by a series of layers, separated by rough interfaces, and each potentially containing suspended scatterers. We deal here only with the single-layer case to illustrate the fundamental issues in subsurface probing.
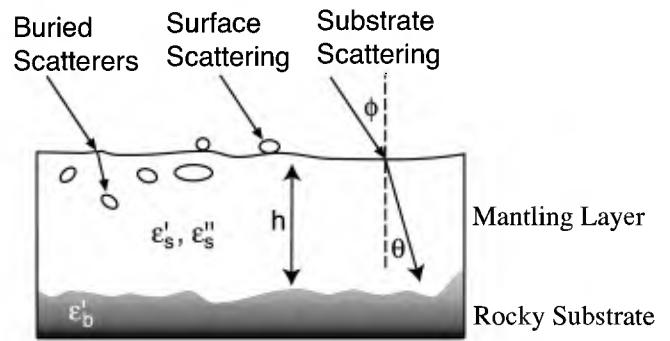

Figure 1. Schematic of the surface and subsurface physical properties discussed in the text.

[7] The range of real dielectric constants for mantling deposits on Mars is likely to be relatively narrow since in dry materials ε' is largely determined by bulk density rather than composition. A range of ε_s' values from ~2.5 to ~4.0 is reasonable for Mars surface dust layers, on the basis of measurements of dry terrestrial and lunar materials. This corresponds to bulk densities of 1.4–2.0 g/cm^3 [*Ulaby et al.*, 1988; *Carrier et al.*, 1991]. Over the range used for radar remote sensing, the loss tangent of most geologic materials is relatively independent of frequency but varies strongly with the volume abundance of particular "lossy" minerals such as ilmenite or hematite [*Ulaby et al.*, 1988]. Low-loss lunar materials such as anorthosite can have $\tan\delta_s \approx 0.001$, but values for mare basalts increase with ilmenite content to a maximum of ~0.10 [*Carrier et al.*, 1991]. There are no direct measurements of Martian dust loss tangent, but this uncertainty has little effect on our analysis of polarization behaviors. We also assume that the magnetic permeability, μ, of the near-surface materials is ~1; the validity of this assumption is likewise not crucial to the polarimetric analysis.

[8] Surface roughness at a dielectric interface is characterized here by the RMS height, h_o, at the scale of the illuminating wavelength, λ. If the surface roughness is self-affine (fractal) over the range of spatial scales of interest for radar scattering, then we may define the wavelength-scaled RMS height, γ, with reference to the Hurst exponent, H, and the RMS height at a reference length scale, L_o:

$$\gamma = \frac{h_o(\lambda)}{\lambda} = h_o(L_o)\left(\frac{\lambda}{L_o}\right)^H \lambda^{-1} = h_o(L_o)L_o^{-H}\lambda^{H-1}, \quad (1)$$

where L_o is typically taken to be 1 m. Fractal surfaces have "roughness" that increases with horizontal length scale, with a power law dependence on H. High-H surfaces are characterized by very rapid increases in roughness with scale, so there are many large "hills." Low-H surfaces appear "flatter" over long distances [*Shepard et al.*, 2001].

[9] Suspended objects, if present, may be treated as small spheres or facets (e.g., buried rocks or rock faces) or linear features (e.g., cracks in ice or the edges of rocks). Rocks are characterized by a range of ellipsoidal shapes, but we assume that their net scattering properties can be described by these two components. Both facets and linear features

may be distributed in size, and we use a power law scaling behavior to describe the volume density, $N(d)$, with units of number/m^3, as a function of length or diameter, d:

$$N(d) = N(d_o) \left(\frac{d}{d_o} \right)^{\beta},$$ (2)

where d_o is some reference scale size. For populations that display self-affine scaling characteristics, β takes on values between -1 and -3 [Turcotte, 1992].

3. Free Parameters in a Multipolarization Radar Measurement

[10] The polarization state of a radar signal is typically referenced to a "linear" or "circular" basis. In the linear basis a transmitted or reflected signal may be decomposed into complex-valued horizontally (H) and vertically (V) polarized components, E_H and E_V. In the circular basis the signal is decomposed into left (L) and right (R) circularly polarized components, E_L and E_R. Any pair of measurements in "orthogonal" polarizations (HH and HV, VV and VH, LL and LR, or RR and RL) forms a Stokes vector, **S** [Mott, 1986]:

$$\mathbf{S} = \begin{bmatrix} \langle |E_H| \rangle^2 + \langle |E_V| \rangle^2 \\ \langle |E_H| \rangle^2 - \langle |E_V| \rangle^2 \\ 2\mathrm{Re}\langle E_H E_V^* \rangle \\ 2\mathrm{Im}\langle E_H E_V^* \rangle \end{bmatrix} = \begin{bmatrix} \langle |E_L| \rangle^2 + \langle |E_R| \rangle^2 \\ 2\mathrm{Re}\langle E_L E_R^* \rangle \\ 2\mathrm{Im}\langle E_L E_R^* \rangle \\ \langle |E_L| \rangle^2 - \langle |E_R| \rangle^2 \end{bmatrix},$$ (3)

where the asterisk denotes the complex conjugate and the brackets denote a time-averaged expectation value. Multipolarization radar systems, such as the NASA/JPL AIRSAR, use the 4 × 4 element Stokes operator, **W**, to define the backscattered power, $P_{received}$, as a function of the transmitted and received polarization [van Zyl et al., 1987]:

$$P_{received} = [S]_{received} [\mathbf{W}] [S]_{transmitted}.$$ (4)

In the linear basis the Stokes operator is composed of real-valued cross products of the complex-valued scattering matrix elements: S_{HH}, S_{VV}, S_{HV}, and S_{VH}, where the letter pairings denote the polarization of the transmit and receive antennas. The scattering matrix relates the scattered electric field components to the incident field:

$$\begin{bmatrix} E_H \\ E_V \end{bmatrix}_{scattered} = \begin{bmatrix} S_{HH} & S_{VH} \\ S_{HV} & S_{VV} \end{bmatrix} * \begin{bmatrix} E_H \\ E_V \end{bmatrix}_{incident}.$$ (5)

When the Stokes operator is radiometrically calibrated, some of these cross products ($S_{HH}S_{HH}^*$, $S_{VV}S_{VV}^*$, $S_{HV}S_{HV}^*$, $S_{VH}S_{VH}^*$) correspond to the backscatter coefficients, σ_{ij}^o, in their respective polarization states, ij. The backscatter coefficient is a dimensionless parameter, defined as the backscatter cross section (m^2) per unit illuminated area [Skolnik, 1980].

[11] While the full Stokes matrix can have 16 independent elements, reciprocity relationships lead to a correspondence between the HV and VH polarization states. This reduces the number of free parameters within the Stokes matrix to nine [van Zyl et al., 1987]. The free parameters are further reduced

by the assumption that certain cross products ($S_{HH}^* S_{HV}$, $S_{VV}^* S_{VH}$) between scattering matrix terms are negligible. Physically, this requires that the scattering elements responsible for "like-polarized" and "cross-polarized" returns have random phase, which appears to be valid for rough geologic surfaces [Ulaby et al., 1987; Freeman et al., 1992].

[12] With these assumptions, there remain only five independent terms in the Stokes operator, which we may write as σ_{HH}^o, σ_{VV}^o, σ_{HV}^o, and the real and imaginary parts of the HH-VV cross product, ($S_{HH}S_{VV}^*$). In some descriptions the real and imaginary components of the cross product are represented by the "HH-VV correlation coefficient" and "mean HH-VV phase." For many natural surfaces the scattering centers are azimuthally isotropic, such that the average HH-VV phase tends toward zero [Ulaby et al., 1987]. This reduces the number of free parameters in the Stokes operator to four, which may be represented by σ_{HH}^o, σ_{VV}^o, and the backscatter coefficients for the two circular polarization states, σ_{LR}^o and σ_{LL}^o [Campbell, 2002]:

$$\sigma_{LR}^o = \frac{1}{4} \left(\sigma_{HH}^o + \sigma_{VV}^o \right) + \frac{1}{2} \mathrm{Re} \left[S_{HH} S_{VV}^* \right],$$ (6)

$$\sigma_{LL}^o = \frac{1}{4} \left(\sigma_{HH}^o + \sigma_{VV}^o \right) + \sigma_{HV}^o - \frac{1}{2} \mathrm{Re} \left[S_{HH} S_{VV}^* \right],$$ (7)

where Re[ ] refers to the real component of a complex value.

[13] Planetary radar observations typically measure the complex orthogonal circular polarization echoes, E_L and E_R. From these data we may obtain four independent parameters: σ_{LL}^o, σ_{LR}^o, and a complex cross correlation. The correlation term is often expressed as a "degree of linear polarization," which increases with the degree of coherence between the circular echoes, and a linear polarization angle, τ [Stacy, 1993; Carter et al., 2004]. We cannot uniquely solve for the copolarized linear scattering parameters (σ_{HH}^o and σ_{VV}^o) from these circular-polarized echoes (Appendix A).

4. Radar Polarization in Rough-Surface Scattering

[14] In order to constrain the behaviors of mantled rough surfaces, we must have limiting behaviors for "bare" surfaces. For a plane, there is no backscattered signal when the radar incidence angle, ϕ, is nonzero (Figure 1). In this case the surface acts only as a dielectric interface for energy scattered from depth. The effect of the interface on this radiation is given by the Fresnel power transmission coefficients for horizontal and vertical polarization [Stratton, 1947]:

$$T_H = \frac{4 \cos\phi \sqrt{\varepsilon_s' - \sin^2\phi}}{\left(\cos\phi + \sqrt{\varepsilon_s' - \sin^2\phi} \right)^2},$$ (8)

$$T_V = \frac{4\varepsilon_s' \cos\phi \sqrt{\varepsilon_s' - \sin^2\phi}}{\left(\varepsilon_s' \cos\phi + \sqrt{\varepsilon_s' - \sin^2\phi} \right)^2}.$$ (9)

The effective incidence angle within the subsurface layer, θ, is (Figure 1)

$$\sin\theta = \left(\frac{\sin\phi}{\sqrt{\varepsilon'_s}}\right). \tag{10}$$

[15] As the surface roughens slightly, we may treat the backscattered field using a small-perturbation model (SPM). For this paper we are primarily concerned with the ratios between echoes in various polarization states. The first-order small-perturbation model predicts that the polarization ratios are a function only of the surface dielectric constant and the incidence angle [Barrick and Peake, 1967]:

$$\frac{\sigma^0_{HH}}{\sigma^0_{VV}} = \frac{\left(\varepsilon'_s\cos\phi + \sqrt{\varepsilon'_s - \sin^2\phi}\right)^4}{\left(\cos\phi + \sqrt{\varepsilon'_s - \sin^2\phi}\right)^4 \left((\varepsilon'_s - 1)\sin^2\phi + \varepsilon'_s\right)^2}, \tag{11}$$

$$\frac{\sigma^0_{LL}}{\sigma^0_{LR}} = \frac{\frac{\sigma^0_{HH}}{\sigma^0_{VV}} + 1 - 2\sqrt{\sigma^0_{HH}/\sigma^0_{VV}}}{\frac{\sigma^0_{HH}}{\sigma^0_{VV}} + 1 + 2\sqrt{\sigma^0_{HH}/\sigma^0_{VV}}}, \tag{12}$$

$$\frac{\sigma^0_{HV}}{\sigma^0_{HH}} = \frac{\sigma^0_{VH}}{\sigma^0_{VV}} = 0. \tag{13}$$

Note that the first-order small-perturbation model predicts no cross-polarized linear component.

[16] The SPM is limited in application to surfaces with roughness, at the scale of the wavelength, on the order of $\lambda/20$ ($\gamma < 0.05$). For surfaces with greater roughness the backscatter from rocky terrain can be decomposed into components with the properties of smooth facets and randomly oriented small dipole elements [Campbell et al., 1993]. For facet or dipole scattering, $\frac{\sigma^0_{HH}}{\sigma^0_{VV}} = 1$. Ratios that involve the cross-polarized linear and the circular-polarized components depend on the relative proportions of "facet" and "dipole" scattering. If we define the contributions of the two mechanisms to the HH or VV echoes as σ^0_{facet} and σ^0_{dipole}, then [Campbell, 2002]

$$\frac{\sigma^0_{LL}}{\sigma^0_{LR}} = \frac{\sigma^0_{dipole}}{\frac{3}{2}\sigma^0_{facet} + \sigma^0_{dipole}}, \tag{14}$$

$$\frac{\sigma^0_{HV}}{\sigma^0_{HH}} = \frac{\sigma^0_{dipole}}{3\left(\sigma^0_{dipole} + \sigma^0_{facet}\right)}. \tag{15}$$

When the dipole mechanism dominates the echo, we obtain maximum polarization ratios of $\sigma^0_{LL}/\sigma^0_{LR} = 1$ and $\sigma^0_{HV}/\sigma^0_{HH} = 1/3$.

[17] The polarization properties of a rough surface are thus dependent on the magnitude (γ) and the physical characteristics (facet-like, dipole-like) of the surface roughness. The transition between the slightly rough surface behavior and that of the facet/dipole model depends, to some degree, on the functional form of the surface roughness power spectrum [Fung et al., 1992; Wu et al., 2001]. Of particular importance here is the relatively low roughness threshold (i.e., $h_o(\lambda)$ near
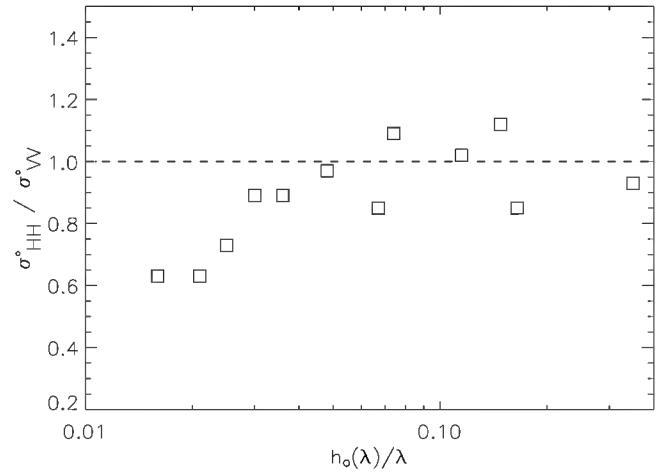

Figure 2. Plot of $\sigma^0_{HH}/\sigma^0_{VV}$ ratio as a function of surface RMS height at the scale of the illuminating wavelength ($h_o(\lambda)/\lambda$, or γ) for Hawaiian lava flows. Radar data from the NASA/JPL AIRSAR; topography data from field measurements.

the $\lambda/20$ limit) between the SPM and "rough surface" models. This transition may be illustrated with AIRSAR data and field topography measurements of Hawaiian lava flows [Campbell and Shepard, 1996; Shepard et al., 2001]. Figure 2 shows the $\sigma^0_{HH}/\sigma^0_{VV}$ ratio as a function of γ for backscatter data at 5.7-, 24-, and 68-cm wavelengths. Each value of γ is derived from topographic profile measurements at the horizontal scale of interest; we have not interpolated upward or downward in scale. These data show that $\sigma^0_{HH}/\sigma^0_{VV} \approx 1$ for $\gamma > 0.05$, consistent with the generally stated limits of the SPM model.

[18] The scattering relationships noted above for "continuous" surfaces also apply to fields of scattering objects (such as rocks), with similar limits on the surface RMS height at the scale of the radar wavelength [Campbell, 2001]. When these objects are jumbled closely together, and are smooth-sided on the scale of the radar wavelength, the surface may be described as "blocky." In this case we observe strong double-bounce reflections from favorably oriented pairs of rock faces. Forward scattering preferentially enhances the horizontally polarized component in the reflected signal, so the $\sigma^0_{HH}/\sigma^0_{VV}$ ratio can exceed unity. Likewise, the two reflection events enhance the same-sense circular echoes (σ^0_{LL} or σ^0_{RR}), so blocky surfaces can exhibit circular polarization ratios greater than unity [Plaut et al., 2004; Campbell et al., 1993; Hagfors and Campbell, 1974].

5. Radar Polarization in Subsurface Scattering

[19] Volume scattering within a mantling layer may be treated by two end-member cases [e.g., Stacy, 1993]. The first assumes facet-like scattering from objects larger than the radar wavelength within the medium, λ', which is smaller than the free-space value:

$$\lambda' = \frac{\lambda}{\sqrt{\varepsilon'_s}}. \tag{16}$$

Such echoes are characterized by equal σ^0_{HH}, σ^0_{VV}, and σ^0_{LR} values, and $\sigma^0_{HV} = \sigma^0_{LL} = 0$ (disregarding momentarily

the role of the upper interface). This behavior is consistent with Mie or geometric optics scattering from spheres [Bohren and Huffman, 1983] and is identical to that of facet-like surface echoes discussed above. The second component assumes a randomly oriented distribution of cracks or highly ellipsoidal objects, whose polarization properties are identical to those of the surface "dipole" component. In practice, the two effects might arise from the same objects, such as mirror-like echoes from smooth rock faces and dipole-like reflections from irregular rock edges. Multiple scattering between buried objects is neglected here, since the increased path length through the lossy medium and the low net reflection coefficient for two successive scattering events from suspended rocks will lead to relatively weak echoes. The similarities between models for surface and subsurface rough interfaces or suspended scatterers are a key element in developing a useful suite of polarimetry analysis tools.

6. Attenuation and Polarimetric Effects of the Mantling Layer

[20] The presence of a homogeneous dielectric mantling layer has several effects on an incident wave. The transmitted angle, θ, is less than ϕ (equation (10)). In many cases the radar backscatter coefficient of a rough interface increases with lower incidence angle, so echoes from a buried surface are enhanced. The wavelength in the mantling layer is also reduced relative to the free-space value (equation (16)). Because self-affine surfaces appear "rougher" to shorter probing wavelengths (equation (1)), this further enhances the reflection from a buried interface. The latter argument also holds for distributed scatterers, which are more numerous at smaller diameters (equation (2)). The received backscattered power from buried interfaces or scatterers is reduced due to the lower effective dielectric contrast between the mantle and the substrate/objects, in contrast to that between a "bare" surface and air or vacuum. Natural materials also have a finite effective conductivity, which imposes a round-trip power loss, A, on the penetrating signal (independent of polarization) as a function of the free-space wavelength, λ, and the layer thickness, h:

$$A(\lambda) = \exp\left[-\frac{8\pi h}{\lambda \cos\theta}\left(\frac{\varepsilon_s'}{2}\left[\sqrt{1 + \tan^2 \delta_s} - 1\right]\right)^{1/2}\right]. \quad (17)$$

[21] The polarimetric influence of the upper surface of the mantling layer on the observed echo may be described by a net (round-trip) transmission coefficient. For buried spheres or dipoles, smooth rock faces, or a faceted basal interface, the HH- and VV-polarized echoes from any given scattering event are identical, so the net coefficients are simply T_H^2 and T_V^2. Radar energy that is changed in polarization by scattering within the mantling layer (e.g., HV-polarized returns from dipole-like objects) has a net transmission coefficient given by $T_H T_V$. The net transmission coefficients, as a function of incidence angle, for a dust layer with $\varepsilon_s' = 4.0$ are shown in Figure 3. For $\phi < 45°$ the variation in echo strength due solely to
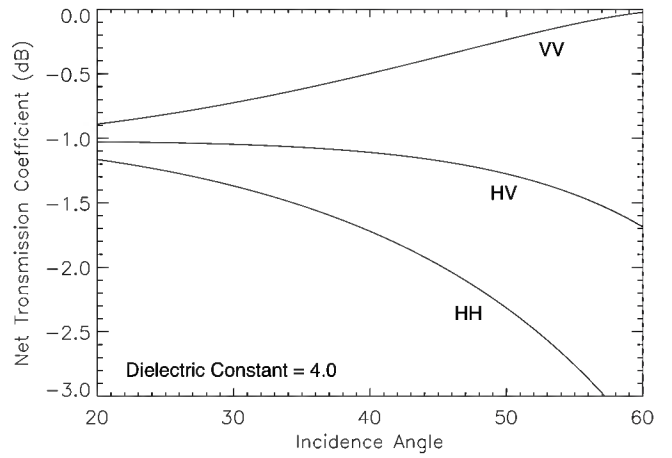

Figure 3. Net transmission coefficients (in dB), as a function of radar incidence angle, for a dielectric interface with $\varepsilon_s' = 4.0$ for HH, VV, and HV polarizations.

transmission effects is no more than $\sim$1.5 dB; reducing ε_s' to 2.5 yields a range of $\sim$1 dB.

[22] The transmission coefficients may be used to define ratios between observed power in various polarizations as a function of the mantling layer dielectric constant and radar incidence angle. We assume in each case that the Fresnel coefficients can be evaluated at the radar incidence angle (i.e., the surface is not highly tilted on horizontal scales $\geq \lambda$). We also ignore the scenario of a buried surface that scatters by the small-perturbation mechanism since the net echo would be very weak. For facet-like and dipole-like subsurface scattering,

$$\frac{\sigma_{HH}^0}{\sigma_{VV}^0} = \frac{T_H^2}{T_V^2}. \quad (18)$$

In our models, only the dipole-like mechanism can produce HV- or VH-polarized echoes, and this component is characterized by

$$\frac{\sigma_{HV}^0}{\sigma_{HH}^0} = \frac{T_V}{3T_H}. \quad (19)$$

The circular-polarized returns may be obtained by determining the HH-VV correlation term in equations (6) and (7) for the particular scattering model. For facet-like scattering,

$$\mathrm{Re}\left[S_{HH}S_{VV}^*\right] = \sqrt{\sigma_{HH}^0 \sigma_{VV}^0}, \quad (20)$$

so

$$\frac{\sigma_{LL}^0}{\sigma_{LR}^0} = \left(\frac{T_H - T_V}{T_H + T_V}\right)^2. \quad (21)$$

Subsurface facet-like reflections, which produce no LL-polarized reflections, have a small net σ_{LL}^0 component due to "stretching" of the polarization ellipse by passage through the surface. For the range of mantling-layer dielectric values considered here, this component is
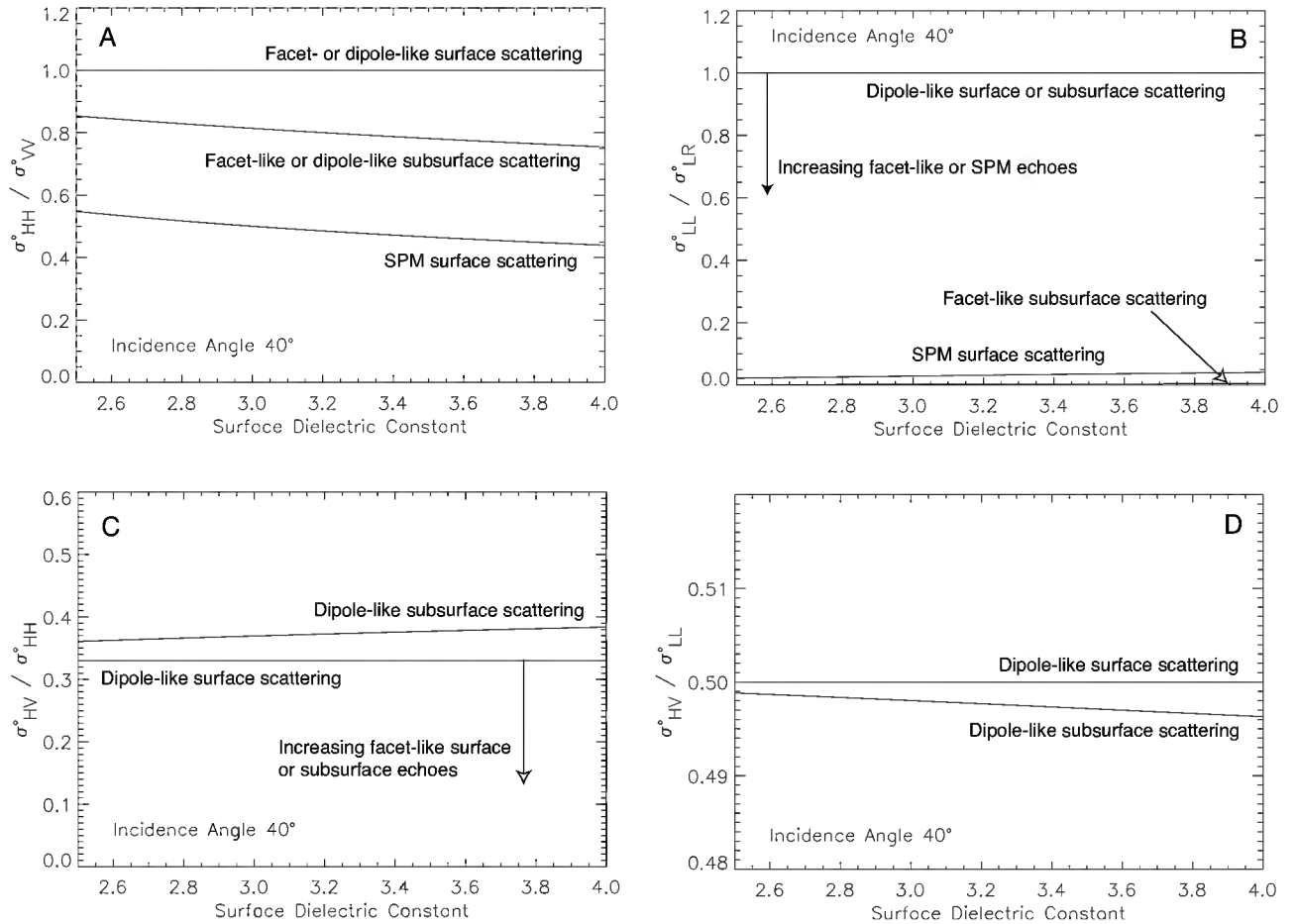
Figure 4. Polarization ratios versus surface dielectric constant as a function of scattering mechanism for radar incidence angle of 40°. Note change of vertical axis scaling for each plot. (a) $\sigma^o_{HH}/\sigma^o_{VV}$ ratio, (b) $\sigma^o_{LL}/\sigma^o_{LR}$ ratio, (c) $\sigma^o_{HV}/\sigma^o_{HH}$ ratio, (d) $\sigma^o_{HV}/\sigma^o_{LL}$ ratio. The latter two plots show that the cross-polarized component is, in general, a product of both surface and subsurface returns.

negligible. For randomly oriented dipole scatterers the HH-VV correlation term is given by

$$\mathrm{Re}\left[S_{HH}S^*_{VV}\right] = \sigma^o_{HV}, \qquad (22)$$

and from equations (6) and (7),

$$\frac{\sigma^o_{LL}}{\sigma^o_{LR}} = 1. \qquad (23)$$

Finally, we examine the $\sigma^o_{HV}/\sigma^o_{LL}$ ratio, which is dominated by the relative contributions of surface and subsurface dipole-like scatterers. Surface and subsurface facet-like returns produce no HV-polarized return and only a very small LL-polarized echo for our range of $\varepsilon'_s(21)$. Combining equations (7), (18), (19), and (22), we obtain

$$\frac{\sigma^o_{HV}}{\sigma^o_{LL}} = \left[\frac{3}{4}\left(\frac{T_H}{T_V} + \frac{T_V}{T_H}\right) + \frac{1}{2}\right]^{-1}. \qquad (24)$$

This ratio has a maximum value of 1/2 when the echoes arise entirely from surface scattering and declines slightly for subsurface reflections when ε'_s is small (e.g., <8).

[23] Figure 4 presents polarization ratios for $\phi = 40°$ as a function of ε'_s. The curves represent the polarimetric behavior of "end-member" scenarios (e.g., purely subsurface dipole-like scattering, purely surface small-perturbation scattering). The $\sigma^o_{HV}/\sigma^o_{HH}$ and $\sigma^o_{HV}/\sigma^o_{LL}$ ratios provide little discrimination between surface and subsurface echoes when ε'_s is relatively small. It is also clear that we cannot assume that the cross-polarized signal arises primarily from subsurface scattering [cf. *Paillou et al.*, 2003]. The $\sigma^o_{HH}/\sigma^o_{VV}$ and $\sigma^o_{LL}/\sigma^o_{LR}$ ratios provide a greater dynamic range for inferring the relative surface and subsurface components. The $\sigma^o_{HH}/\sigma^o_{VV}$ parameter, however, has advantages over $\sigma^o_{LL}/\sigma^o_{LR}$ in that the relative proportions of facet-like and dipole-like echoes (surface or subsurface) do not affect the former ratio. If our assumptions regarding the scattering properties of the mantled surface are valid, then the $\sigma^o_{HH}/\sigma^o_{VV}$ ratio provides the best means to determine the fraction of subsurface return over a plausible range of ε'.

7. Implications for Mars Orbital Radar Studies

[24] In this section we assess the implications of the above analyses for the design of a Mars orbital radar sensor.

Our results are divided into sections that parallel the science goals of such a system.

7.1. Identify Buried Rough Terrain

[25] The most obvious goal of a Mars orbital SAR is to map geologic features buried by dust or sand. The major system design parameters are the radar wavelength, polarization, and sensitivity, with the optimum choice guided by a number of trade-offs.

[26] The choice of VV polarization to minimize transmission losses, and thus maximize penetration depth, is straightforward (Figure 3). There are relatively few terrestrial examples of surfaces so blocky that σ^0_{HH} is significantly greater than σ^0_{VV}; only in such a case might the HH polarization be preferable for probing buried terrain [Campbell et al., 1993]. HV polarization is less desirable because even very rough surfaces reach a maximum of only $\sigma^0_{HV}/\sigma^0_{VV} \approx 1/3$ [Campbell, 2002]. The consequent loss of 5 dB or more in backscatter strength from a buried surface, relative to the VV return, considerably reduces the effective depth of detection.

[27] The depth of radar penetration increases with λ (equation (17)), but for most natural surfaces the wavelength-scale roughness, and thus σ^0, declines with λ (equation (1)). In addition, for a given antenna diameter, the total transmit/receive gain declines as λ^{-2} [Skolnik, 1980]. These three effects may be represented by

$$\frac{P}{P_r} \propto \frac{\lambda^{-2}\left(1 - \exp\left[-a\lambda'^{(2H-2)}\right]\right)\exp\left[\frac{-b}{\lambda}\right]}{\lambda_r^{-2}\left(1 - \exp\left[-a\lambda_r'^{(2H-2)}\right]\right)\exp\left[\frac{-b}{\lambda_r}\right]}. \tag{25}$$

P/P_r is the ratio of received power at wavelength λ to that at a reference wavelength, λ_r (all scaling terms related to antenna size, range to the target, transmitted power, receiver properties, and area of an image resolution cell are assumed constant). The first term in the right numerator and denominator represents antenna gain. The second term represents the change in wavelength-scale surface roughness, using a functional form typical of self-affine terrain; a is an empirically derived constant for a particular polarization and incidence angle [Campbell and Shepard, 1996]. Note that the wavelength term in the roughness expression is modified for the effects of the dielectric mantle (equation (16)). The third term represents attenuation in the mantling layer; b is a function of the loss tangent and mantle depth (equation (17)).

[28] We may illustrate the importance of probing wavelength using an example case. Assume that we wish to detect a moderately rough surface (RMS slope of 10° at 1-m scale, $H = 0.5$) beneath 3 m of dust with a real dielectric constant of 3.0, using a radar incidence angle of 40° and VV polarization. On the basis of empirical data for Hawaiian lava flows, the value of a in this case is ~0.33. If we use a 12.6-cm (S band) radar wavelength for λ_r, then we may plot the backscatter coefficient enhancement as a function of free-space λ and the loss tangent of the dust. Figure 5 shows the results for $\tan\delta = 0.005$, 0.01, and 0.02.

[29] Inspection of equation (25) shows that for moderate mantle thicknesses and loss tangents, the relative attenuation change with λ dominates the result. For
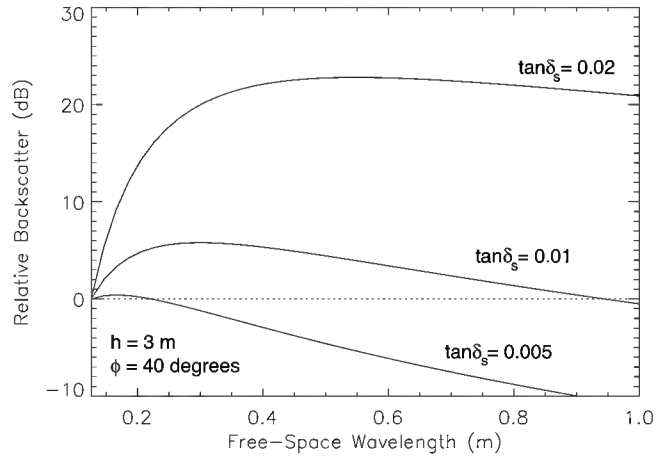

Figure 5. Plot of backscatter enhancement (in dB) for a buried, moderately rough surface (10° RMS slope at 1-m scale, $H = 0.5$) as a function of free-space radar wavelength. Dust mantle thickness 3 m, real dielectric constant 3.0, and loss tangent as noted. VV polarization, radar incidence angle 40°. Backscatter normalized to 0 dB at 12.6-cm wavelength. Positive values of backscatter enhancement therefore correspond to stronger echoes, relative to the 12.6-cm return.

smaller values of $\tan\delta$, thinner layers, or smoother substrates, the antenna gain and roughness-related losses eventually exceed any benefit of increasing wavelength. When $\tan\delta = 0.005$, there is a decline in effective backscatter, relative to $\lambda_r = 12.6$ cm, for $\lambda > 20$ cm (Figure 5). As the loss tangent of the dust increases, the attenuation component dominates the result, and the improvement in subsurface feature detection reaches a maximum value at progressively longer wavelengths. The "ideal" wavelength is therefore a compromise: we wish to detect rough interfaces beneath deep or lossy mantles but not to greatly reduce the echoes from features beneath shallow or low-loss layers. On the basis of the examples shown in Figure 5, and the wide range of possible loss tangent values for Mars mantling materials, P band (frequency ~1 GHz or less, $\lambda \approx 30$ cm or longer) observations offer the greatest potential for characterizing buried features over this range of mantling layer properties.

7.2. Constrain the Subsurface Echo Component

[30] In a geologically complex setting, it may not be immediately evident that a radar-mapped feature is exposed at the surface or buried by mantling material. The second major goal of a Mars orbital radar is thus to constrain the surface and subsurface echo components, which may be accomplished using polarimetric data.

[31] On the basis of the results of section 6, the $\sigma^0_{HH}/\sigma^0_{VV}$ ratio is the best choice if only two measurements can be obtained. If $\sigma^0_{HH}/\sigma^0_{VV} \approx 1$, we cannot obtain quantitative information about subsurface echoes; while subsurface scattering may occur, the rough surface either dominates the echo or jumbles the polarization of the transmitted radiation. When $\sigma^0_{HH}/\sigma^0_{VV} > 1$, we may infer surface blocky texture on scales greater than the radar wavelength. The most useful case for our interests
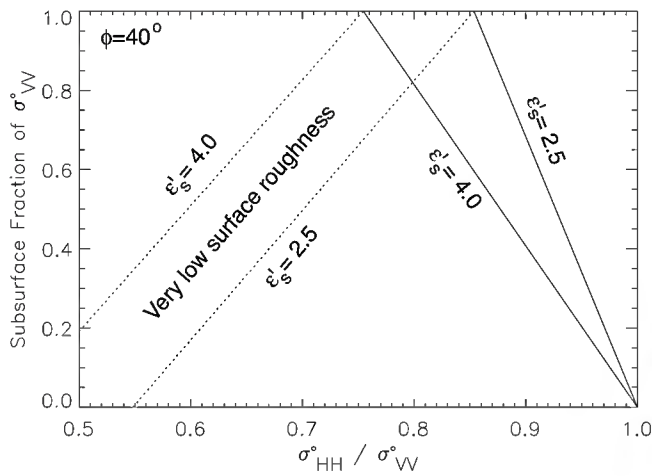
Figure 6. Fraction of σ^0_{VV} arising from the subsurface, as a function of $\sigma^0_{HH}/\sigma^0_{VV}$, for mantling layer dielectric constant of 2.5 and 4.0, using a model that assumes surface roughness satisfies the small-perturbation model condition (dashed lines), and a model that assumes surface roughness exceeds the small-perturbation model criterion (solid lines). Radar incidence angle 40°.

requires $\sigma^0_{HH}/\sigma^0_{VV} < 1$. In this instance the specific analysis approach depends on the magnitude of the wavelength-scale surface roughness, γ. For a Mars orbital radar system the most likely source for this additional information will be surface rock-abundance estimates from thermal-infrared data [*Christensen*, 1986], with additional guidance from high-resolution photography.

[32] If the surface is exceedingly smooth (e.g., very low rock abundance and minimal structure at the meter scale), we may obtain an estimate of the subsurface fraction of the VV echo as a function of the mantling layer dielectric constant, ε'_s:

$$F_{\text{subsurface-VV}} = \frac{\left(\frac{\sigma^0_{HH-SPM}}{\sigma^0_{VV-SPM}} - \frac{\sigma^0_{HH}}{\sigma^0_{VV}} \right)}{\left(\frac{\sigma^0_{HH-SPM}}{\sigma^0_{VV-SPM}} - \frac{T^2_H}{T^2_V} \right)}, \quad (26)$$

where the ratio of SPM components is given by equation (11). A similar approach applies when the surface exceeds the roughness limits of the SPM ($\gamma > 0.05$). In this case the surface-scattered component is characterized by $\sigma^0_{HH}/\sigma^0_{VV} = 1$, and the subsurface fraction of σ^0_{VV}, as a function of ε'_s, is

$$F_{\text{subsurface-VV}} = \frac{\left(1 - \frac{\sigma^0_{HH}}{\sigma^0_{VV}} \right)}{\left(1 - \frac{T^2_H}{T^2_V} \right)}. \quad (27)$$

Values for the subsurface fraction of σ^0_{VV} as a function of $\sigma^0_{HH}/\sigma^0_{VV}$ and ε'_s are shown in Figure 6 (for $\phi = 40°$). As expected from Figure 4a, the likely range in $\sigma^0_{HH}/\sigma^0_{VV}$ for Mars observations is relatively small, particularly for the more likely scenario of surface roughness with $\gamma > 0.05$. Any potential polarimetric system must thus be very well calibrated, with HH-VV channel balance better than 0.5 dB. HH-VV uncertainties at the 0.6- to 0.7-dB level were achieved for the actively steered SIR-C system, and

use of a fixed look angle and a passive antenna for a Mars orbital radar should permit more accurate calibration [*Freeman et al.*, 1995].

[33] P band AIRSAR data provide examples of this technique for Mars-analog terrestrial sites. We choose three terrain types: lava flows in Hawaii [*Campbell and Shepard*, 1996], the Lavic Lake playa (Figure 7a), and a smooth-surfaced portion of the Keanakakoi ash near Kilauea caldera, Hawaii (Figure 7b). For the latter deposit we collected a ground-penetrating radar transect using a 500-MHz system
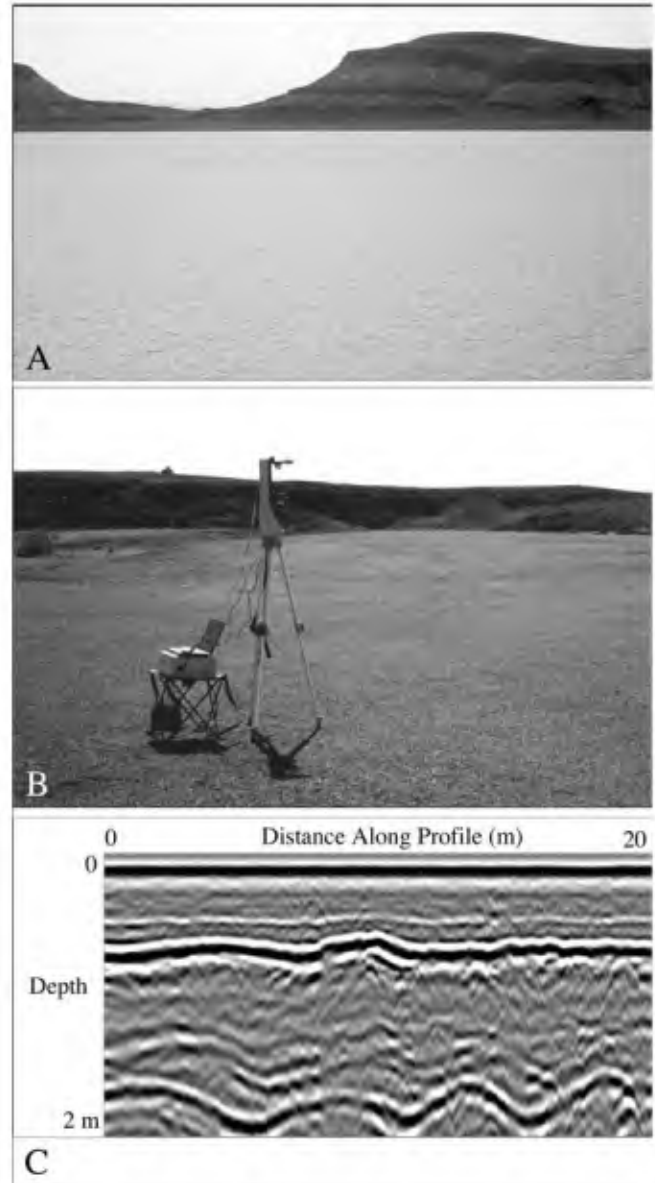

Figure 7. (a) Field photo of the Lavic Lake playa, showing polygonal crack pattern in an otherwise very smooth surface. (b) A portion of the Keanakakoi ash deposit near Kilauea caldera, Hawaii. Tripod supports a high-resolution laser topography measurement system. (c) Ground-penetrating radar transect of the ash site, using a radar frequency of 500 MHz (P band). The vertical exaggeration is about 10, so the two evident subsurface horizons are considerably less rugged than implied here.
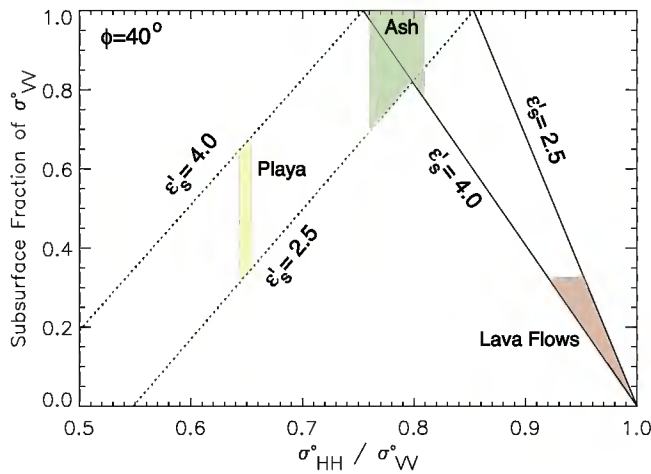
Figure 8. Polarization ratios for field sites shown as shaded intersections with model presented in Figure 6.

that is very close in wavelength to the P band AIRSAR channel (Figure 7c). On the basis of field measurements of topography, the playa and ash surfaces have RMS heights at 68-cm horizontal scale of 0.6–0.7 cm, so $\gamma \approx 0.01$. The lava flows are characterized by $\gamma > 0.2$ [*Shepard et al.*, 2001]. Figure 8 shows the intersection of the P band $\sigma^o_{HH}/\sigma^o_{VV}$ ratios for these sites with the models proposed above. As expected, the lava flows are characterized by low subsurface scattering components. The ash deposit, which has strong reflecting horizons (possibly cemented layers) within 2 m of the surface, has a polarization ratio consistent with a nearly planar upper interface. The playa appears to have a larger surface echo component than the ash, perhaps due to the presence of polygonal cracks that act as scattering centers. This example shows that a considerable amount of information about surface and subsurface geologic properties may be obtained from a simple polarization ratio measurement.

7.3. Thickness of Mantling Material

[34] A third science goal for a Mars radar mission is to constrain the thickness of surficial material as a guide to understanding aeolian, fluvial, impact, or volcanic deposition/transport processes. Radar could potentially address this issue through multiwavelength or interferometric observations.

[35] Assume a simple case of a rough interface buried by a fine-grained dust layer. If σ^o_{VV} values are obtained at two wavelengths, λ_1 and λ_2, their ratio may be expressed as the sum of the surface and subsurface returns:

$$\frac{\sigma^o_{VV}(\lambda_2)}{\sigma^o_{VV}(\lambda_1)} = \frac{\sigma^o_{VV-surface}(\lambda_2) + \sigma^o_{VV-subsurface}(\lambda_2)}{\sigma^o_{VV-surface}(\lambda_1) + \sigma^o_{VV-subsurface}(\lambda_1)}. \quad (28)$$

On the basis of the models above, a general description for this scenario requires knowledge of the roughness parameters $(H, h_0(L_o))$ for the surface and subsurface interfaces, ε'_s and $\tan\delta_s$, and the thickness of the mantling material, h. Clearly, this situation is too underdetermined to permit useful inferences about the properties of the dust mantle. We may remove some of the complexity by measuring σ^o_{HH} at

both wavelengths and using equation (26) or (27) to determine the subsurface echo component, F. In this case, equation (28) may be written as

$$\frac{F(\lambda_2)\sigma^o_{VV}(\lambda_2)}{F(\lambda_1)\sigma^o_{VV}(\lambda_1)} = \frac{\sigma^o_{VV-subsurface}(\lambda_2)}{\sigma^o_{VV-subsurface}(\lambda_1)}$$
$$= \frac{A(\lambda_2)\left(1 - \exp\left[-a\lambda_2^{\prime(2H-2)}\right]\right)}{A(\lambda_1)\left(1 - \exp\left[-a\lambda_1^{\prime(2H-2)}\right]\right)}, \quad (29)$$

where $A(\lambda)$ represents attenuation at a particular wavelength (equation (17)), and we again use a general expression for the dependence of substrate roughness/backscatter on wavelength. The attenuation is dependent on ε'_s, $\tan\delta_s$ and h, while the backscatter variation with λ is represented by a and H.

[36] Since we cannot measure the roughness parameters of the subsurface interface, there is only one scenario that yields useful information on the mantling deposit. If $H = 1$ for the buried interface, corresponding to a surface that is uniformly rough over the wavelength range of interest (e.g., a rugged fluvial channel floor or lava flow), then equation (29) yields

$$\frac{F(\lambda_2)\sigma^o_{VV}(\lambda_2)}{F(\lambda_1)\sigma^o_{VV}(\lambda_1)} = \frac{A(\lambda_2)}{A(\lambda_1)}$$
$$= \exp\left[\frac{-8\pi h}{\cos\theta}\left(\frac{\varepsilon'_s}{2}\left[\sqrt{1+\tan^2\delta}-1\right]\right)^{1/2}\left(\frac{1}{\lambda_2}-\frac{1}{\lambda_1}\right)\right]. \quad (30)$$

Given ϕ, λ_1, λ_2, and a relatively narrow range for ε'_s, we arrive at an expression that links the observed parameters to the thickness and loss tangent of the dust. Even for this idealized case, and measuring four σ^o values, we cannot decouple the effects of these two parameters. Given the wide possible range of $\tan\delta$ values for Martian surface materials, it does not appear that multiwavelength polarimetric data can provide a strong constraint on mantle layer thickness.

[37] More robust estimates of h may be obtained by interferometric correlation of radar data collected on suitably spaced orbit tracks. This technique exploits the fact that the distribution of phase values for two observations increases with the size of the scattering region along the radar delay (or range) axis. Mapping of ice sheet thickness using phase decorrelation has been demonstrated [*Hoen and Zebker*, 2000]. For Mars dust thickness estimation, the desired accuracy is on the order of perhaps 1 m, so the required phase measurement accuracy and interferometric baseline control will likely be challenging.

8. Summary and Conclusions

[38] Using the most simplistic reasonable model for the Martian near-surface environment, our analyses show how polarimetric data may be used to infer surface and subsurface geologic characteristics. They also reveal specific limitations on the value of various polarization ratios, especially in the context of finite limits on channel gain calibration (e.g., detecting very small shifts in the $\sigma^o_{HV}/\sigma^o_{LL}$

ratio may exceed plausible system calibration targets). On the basis of our results, we suggest the following design criteria for a Mars orbital imaging radar system.

[39] (1) Mapping of buried geologic features is best accomplished using VV polarization, at an optimal wavelength determined by the competing effects of antenna gain, attenuation in the dust, and the reduction in effective surface roughness with wavelength. For reasonable values of dust depth and loss properties, P band frequencies ($\sim$1 GHz or less) offer the best opportunity for detection of moderately rough, buried features. (2) The relative roles of surface and subsurface scattering may be determined using measurements in HH and VV polarization, with a requisite channel gain calibration better than 0.5 dB. (3) The thickness of a mantling layer (or ice mass) cannot be directly inferred from multiwavelength observations; even for HH and VV measurements in two wavelengths, we obtain only an estimate of the combined effects of dust thickness and loss tangent. However, mantle or ice layer thickness may be inferred from the interferometric correlation of backscatter measurements in a single polarization collected on suitably spaced orbital passes. While additional information may be gained by collecting scattering data in more polarizations or wavelengths, we suggest that the primary science goals of a Mars orbital radar could be accomplished by a single-wavelength, P band system capable of collecting VV and HH polarizations with the calibration and orbit control needed to permit interferometric analysis.

Appendix A: Relationship of Linear and Circular Polarization Echo Measurements

[40] This section shows the relationship between dual-circular polarization measurements (E_L and E_R) and the linear-basis scattering parameters. For an illuminating wave that is right circular polarized, the reflected wave Stokes vector, [Q], is

$$\begin{bmatrix} Q_0 \\ Q_1 \\ Q_2 \\ Q_3 \end{bmatrix} = [M] \begin{bmatrix} 1 \\ 0 \\ 0 \\ -1 \end{bmatrix} = \begin{bmatrix} M_{11} - M_{14} \\ M_{12} - M_{24} \\ M_{13} - M_{34} \\ M_{14} - M_{44} \end{bmatrix}, \quad (A1)$$

where [M] is the Mueller matrix, which in the linear basis is composed of cross products of the complex scattering matrix elements, S_{HH}, S_{VV}, and $S_{HV} = S_{VH}$. The fraction of the total echo power that has a deterministic linear polarization, D, is

$$D = \frac{\sqrt{Q_1^2 + Q_2^2}}{Q_0} = \frac{\left[(M_{12} - M_{24})^2 + (M_{13} - M_{34})^2\right]^{1/2}}{M_{11} - M_{14}}, \quad (A2)$$

and the orientation angle of the polarization ellipse, τ, is

$$\tau = \frac{1}{2}\tan^{-1}\left(\frac{Q_2}{Q_1}\right) = \frac{1}{2}\tan^{-1}\left(\frac{M_{13} - M_{34}}{M_{12} - M_{24}}\right). \quad (A3)$$

[41] As discussed in section 3, the copolarized and cross-polarized linear echoes have random phase, such that $\langle S_{HH}S_{HV}^* \rangle = \langle S_{VV}S_{VH}^* \rangle = 0$ [Ulaby et al., 1987; Freeman et al., 1992]. This assumption is violated when a volume-

scattering target surface is tilted along the azimuth direction, since the subsurface echo comprises correlated H- and V-polarized components with deterministic phase. In this case the polarization ellipse orientation angle may be used to infer the surface slope [Stacy, 1993; Lee et al., 2000].

[42] If there is no significant surface tilt along the azimuth axis, then inserting the remaining nonzero Mueller matrix elements in equations (A2) and (A3) yields

$$D = \frac{\sqrt{(\sigma_{HH}^0 - \sigma_{VV}^0)^2 + 4\text{Im}(S_{HH}S_{VV}^*)^2}}{\sigma_{HH}^0 + \sigma_{VV}^0 + 2\sigma_{HV}^0}, \quad (A4)$$

$$\tau = \frac{1}{2}\tan^{-1}\left[\frac{2\text{Im}(S_{HH}S_{VV}^*)}{\sigma_{HH}^0 - \sigma_{VV}^0}\right]. \quad (A5)$$

For the facet-like and diffuse (dipole-like) scattering models, the imaginary component of the HH-VV correlation term is zero [e.g., Ulaby et al., 1987]. As a result, the derived polarization orientation angle is zero for an H- ($\tau = 0°$) or V-polarized ($\tau = 90°$) echo; the specific value of τ is retained in the sign of the Q_1 term. In this case the degree of linear polarization simplifies to

$$D = \frac{|\sigma_{HH}^0 - \sigma_{VV}^0|}{(\sigma_{HH}^0 + \sigma_{VV}^0 + 2\sigma_{HV}^0)}. \quad (A6)$$

So we see that D captures the difference between σ_{HH}^0 and σ_{VV}^0 relative to the "span" or total scattered power from the surface. The fourth Stokes vector term is given by

$$Q_3 = \sigma_{LR}^0 - \sigma_{LL}^0 = \text{Re}\langle S_{HH}S_{VV}^* \rangle - \sigma_{HV}^0. \quad (A7)$$

For facet-like scatterers, $\text{Re}\langle S_{HH}S_{VV}^* \rangle = \sqrt{\sigma_{HH}^0\sigma_{VV}^0}$, and for randomly oriented dipoles, $\text{Re}\langle S_{HH}S_{VV}^* \rangle = \sigma_{HV}^0$. Because we cannot solve explicitly for σ_{HV}^0, measurements in dual-circular polarization cannot be used to derive the $\sigma_{HH}^0/\sigma_{VV}^0$ ratio.

References

Barrick, D. E., and W. H. Peake (1967), Scattering from surfaces with different roughness scales: Analysis and interpretation, Electrosci. Lab. Rep. 1388–26, Ohio State Univ., Columbus.
Bohren, C. F., and D. R. Huffman (1983), Scattering and Emission From Small Particles, John Wiley, Hoboken, N. J.
Campbell, B. A. (2001), Radar backscatter from Mars: Properties of rock-strewn surfaces, Icarus, 150, 38–47.
Campbell, B. A. (2002), Radar Remote Sensing of Planetary Surfaces, Cambridge Univ. Press, New York.
Campbell, B. A., and M. K. Shepard (1996), Lava flow surface roughness and depolarized radar scattering, J. Geophys. Res., 101, 18,941–18,951.
Campbell, B. A., R. E. Arvidson, and M. K. Shepard (1993), Radar polarization properties of volcanic and playa surfaces: Applications to terrestrial remote sensing and Venus data interpretation, J. Geophys. Res., 98, 17,099–17,113.
Campbell, B. A., D. B. Campbell, J. A. Grant, S. Hensley, T. A. Maxwell, J. J. Plaut, P. Rosen, M. K. Shepard, and R. Simpson (2001), Orbital imaging radar and the search for water on Mars, paper presented at

Conference on the Geophysical Detection of Subsurface Water on Mars, Lunar and Planet. Sci., Houston, Tex.

Campbell, B. A., A. Freeman, L. Veilleux, B. Huneycutt, M. Jones, and R. Shotwell (2004), A P-band radar mission to Mars, paper presented at IEEE Aerospace Conference, Inst. of Electr. and Electron. Eng., Big Sky, Mont.

Carrier, W. D., G. R. Olhoeft, and W. Mendell (1991), Physical properties of the lunar surface, in *Lunar Sourcebook*, pp. 475–594, Cambridge Univ. Press, New York.

Carter, L. M., D. B. Campbell, and B. A. Campbell (2004), Impact crater related surficial deposits on Venus: Multipolarization radar observations with Arecibo, *J. Geophys. Res.*, *109*, E06009, doi:10.1029/2003JE002227.

Christensen, P. R. (1986), The spatial distribution of rocks on Mars, *Icarus*, *68*, 217–238.

Farr, T. G., C. Elachi, P. Hartl, and K. Chowdhury (1986), Microwave penetration and attenuation in desert soil: A field experiment with the SIR, *IEEE Trans. Geosci. Remote Sens.*, *24*, 590–594.

Freeman, A., J. J. van Zyl, J. D. Klein, H. A. Zebker, and Y. Shen (1992), Calibration of Stokes and scattering matrix format polarimetric SAR data, *IEEE Trans. Geosci. Remote Sens.*, *30*, 531–539.

Freeman, A., M. Alves, B. Chapman, J. Cruz, Y. Kim, S. Shaffer, J. Sun, E. Turner, and K. Sarabandi (1995), SIR-C data quality and calibration results, *IEEE Trans. Geosci. Remote Sens.*, *33*, 848–857.

Fung, A. K., Z. Li, and K. S. Chen (1992), Backscattering from a randomly rough dielectric surface, *IEEE Trans. Geosci. Remote Sens.*, *30*, 356–369.

Hagfors, T., and D. B. Campbell (1974), Radar backscattering from Venus at a wavelength of 70 cm, *Astron. J.*, *79*, 493–501.

Haldemann, A. F. C., and D. O. Muhleman (1999), Circular-polarization radar properties of high-altitude ice: Western Kunlun Shan and central Andes, *J. Geophys. Res.*, *104*, 24,075–24,094.

Harmon, J. K., et al. (1994), Radar mapping of Mercury's polar anomalies, *Nature*, *369*, 213–215.

Hoen, E. W., and H. A. Zebker (2000), Penetration depths inferred from interferometric volume decorrelation observed over the Greenland ice sheet, *IEEE Trans. Geosci. Remote Sens.*, *38*, 2571–2583.

Lee, J. S., D. L. Schuler, and T. L. Ainsworth (2000), Polarimetric SAR data compensation for terrain azimuth slope variation, *IEEE Trans. Geosci. Remote Sens.*, *38*, 2153–2163.

Mott, H. (1986), *Polarization in Antennas and Radar*, John Wiley, Hoboken, N. J.

Muhleman, D. O., B. J. Butler, A. W. Grossman, and M. A. Slade (1991), Radar images of Mars, *Science*, *253*, 1508–1513.

Ostro, S. J., et al. (1992), Europa, Ganymede, and Callisto: New radar results from Arecibo and Goldstone, *J. Geophys. Res.*, *97*, 13,091–13,102.

Paillou, P., G. Grandjean, N. Baghdadi, E. Heggy, T. August-Bernex, and J. Achache (2003), Subsurface imaging in south-central Egypt using low-frequency radar: Bir Safsaf revisited, *IEEE Trans. Geosci. Remote Sens.*, *41*, 1672–1684.

Plaut, J. J., S. W. Anderson, D. A. Crown, E. R. Stofan, and J. J. van Zyl (2004), The unique radar properties of silicic lava domes, *J. Geophys. Res.*, *109*, E03001, doi:10.1029/2002JE002017.

Schaber, G. G., T. W. Thompson, and S. H. Zisk (1975), Lava flows in Mare Imbrium: An evaluation of anomalously low Earth-based radar reflectivity, *Moon*, *13*, 395–423.

Schaber, G. G., J. F. McCauley, C. S. Breed, and G. R. Olhoefl (1986), Shuttle Imaging Radar: Physical controls on signal penetration and subsurface scattering in the eastern Sahara, *IEEE Trans. Geosci. Remote Sens.*, *24*, 603–623.

Schaber, G. G., J. F. McCauley, and C. S. Breed (1997), The use of multi-frequency and polarimetric SIR-C/X-SAR data in geologic studies of Bir Safsaf, Egypt, *Remote Sens. Environ.*, *59*, 337–363.

Shepard, M. K., B. A. Campbell, M. Bulmer, T. Farr, L. R. Gaddis, and J. Plaut (2001), The roughness of natural terrain: A planetary and remote sensing perspective, *J. Geophys. Res.*, *106*, 32,777–32,795.

Skolnik, M. L. (1980), *Introduction to Radar Systems*, McGraw-Hill, New York.

Stacy, N. J. S. (1993), High-resolution synthetic aperture radar observations of the Moon, Ph.D. thesis, Cornell Univ., Ithaca, N. Y.

Stratton, J. A. (1947), *Electromagnetic Theory*, John Wiley, Hoboken, N. J.

Thompson, T. W., W. J. Roberts, W. K. Hartmann, R. W. Shorthill, and S. H. Zisk (1979), Blocky craters: Implications about the lunar megaregolith, *Moon Planets*, *21*, 319–342.

Turcotte, D. L. (1992), *Fractals and Chaos in Geology and Geophysics*, Cambridge Univ. Press, New York.

Ulaby, F. T., R. K. Moore, and A. K. Fung (1982), *Microwave Remote Sensing*, Addison-Wesley-Longman, Reading, Mass.

Ulaby, F. T., D. Held, M. C. Dobson, K. C. McDonald, and T. B. Senior (1987), Relating polarization phase difference of SAR signals to scene properties, *IEEE Trans. Geosci. Remote Sens.*, *25*, 83–91.

Ulaby, F. T., et al. (1988), Microwave dielectric spectrum of rocks, *Radiat. Lab Rep. 23817-1-TU*, Univ. of Mich., Ann Arbor.

van Zyl, J. J., H. A. Zebker, and C. Elachi (1987), Imaging radar polarization signatures: Theory and observations, *Radio Sci.*, *22*, 529–543.

Williams, K. K., and R. Greeley (2001), Radar attenuation by sand: Laboratory measurements of radar transmission, *IEEE Trans. Geosci. Remote Sens.*, *39*, 2521–2526.

Wu, T., K. S. Chen, J. Shi, and A. K. Fung (2001), A transition model for the reflection coefficient in surface scattering, *IEEE Trans. Geosci. Remote Sens.*, *39*, 2040–2050.

———————————

B. A. Campbell and T. A. Maxwell, Center for Earth and Planetary Studies, Smithsonian Institution, Washington, DC 20560-0315, USA. (campbellb@nasm.si.edu)

A. Freeman, Jet Propulsion Laboratory, 4800 Oak Grove Drive, Pasadena, CA 91109, USA.